Quantum confined Tomonaga-Luttinger liquid in Mo_6Se_6 nanowires converted from epitaxial $MoSe_2$ monolayer

Yipu Xia,[†,‡] Bo Wang,[∥,‡] Junqiu Zhang, [†,‡] Yuanjun Jin, [†,§] Hao Tian, [†,§] Wingkin Ho, [†] Hu Xu, [§] Chuanhong Jin[∥,] and Maohai Xie[†,*]*

[†]Physics Department, the University of Hong Kong, Pokfulam Road, Hong Kong

[∥]State Key Laboratory of Silicon Materials, School of Materials and Engineering, Zhejiang University, Hangzhou, Zhejiang, 310027, China

[§]Department of Physics, Southern University of Science and Technology, Shenzhen, Guangdong 518055, China

[‡]These authors contributed equally to this paper.

[*]Corresponding authors, Emails: chhjin@zju.edu.cn (CHJ), mhxie@hku.hk (MHX).

ABSTRACT

Confining interacting particles in one-dimension (1D) changes the electronic behavior of the system fundamentally, which has been studied extensively in the past. Examples of 1D metallic systems include carbon nanotubes, quasi-1D organic conductors, metal chains and domain boundary defects in monolayer thick transition-metal dichalcogenides such as $MoSe_2$. Here single and bundles of Mo_6Se_6 nanowires were fabricated though annealing $MoSe_2$ monolayer grown by molecular-beam epitaxy on graphene. Conversion from two-dimensional (2D) $MoSe_2$ film to 1D Mo_6Se_6 nanowire is reversible. Mo_6Se_6 nanowires form preferentially at the Se-terminated zigzag edges of $MoSe_2$ and stitch to it via two distinct atomic configurations. Mo_6Se_6 wire is metallic and its length is tunable, which represents one of few 1D systems that exhibit properties pertinent to quantum confined Tomonaga-Luttinger liquid, as evidenced by scanning tunneling microscopic and spectroscopic studies.

Electronic behavior of particles confined in one-dimension (1D) is of fundamental interests, which has been intensively studied in the past decades, such as that in carbon nanotubes,[1-4] semiconductor nanowires,[5-8] metal chains,[9, 10] and quasi-1D organic conductors.[11] Indeed, 1D metals are prone to metal-insulator phase transition at low-temperature due to the Peierls instability.[12-14] Electron-electron interaction in 1D systems invalidates the Landau description of the Fermi-liquid and is appropriately described by the Tomonaga-Luttinger liquid (TLL) theory of collective excitations.[15, 16] The hallmark of the TLL includes spin-charge separation and power-law suppression of the electronic density-of-states (DOS) at Fermi energy,[17, 18] which has been reportedly observed in a number of 1D or quasi-1D systems such as carbon nanotubes,[1, 19, 20] purple bronze ($Li_{0.9}Mo_6O_{17}$) crystals,[21, 22] metallic atomic chains,[9, 10] twin domain boundaries in transition-metal dichalcogenide (TMD) monolayers (MLs),[23, 24] as well as the edge states of quantum hall systems.[25, 26] Here, we report a highly controllable and reproducible process of 1D Mo_6Se_6 nanowire fabrication by converting a $MoSe_2$ ML through annealing, which is found to host quantized TLL states as characterized by low-temperature scanning tunneling spectroscopy (STS). The $MoSe_2$ ML is grown by molecular-beam epitaxy (MBE) on graphene or highly oriented pyrolytic graphite (HOPG), and the Mo_6Se_6 nanowires converted from $MoSe_2$ are found to terminate the 2D $MoSe_2$ sheet, providing a new edge structure and modifying the electronic and catalytic properties of the TMDs, for examples. The conversion of Mo_6Se_6 nanowires from $MoSe_2$ is reversible by annealing with or without the supply of selenium. Measurements by scanning tunneling microscopy (STM) and scanning transmission electron microscopy (STEM) establish the atomic structure of Mo_6Se_6 nanowires, the interfaces between the 1D Mo_6Se_6 wire

and 2D $MoSe_2$ sheet, and the electronic characteristics pertinent to the quantum confinement effect and the TLL. The Peierls type charge density wave (CDW) is not observed. These 1D Mo_6Se_6 wires provide another ideal system for studying the physics of interacting electrons in 1D.

Post-growth annealing of an epitaxial $MoSe_2$ ML at $\geq 800°C$ leads to the nucleation and growth of 1D Mo_6Se_6 nanowires at the edges of $MoSe_2$ domains or islands. The $MoSe_2$ film was grown by MBE on SiC-supported graphene or HOPG substrate and Figure 1a presents a reflection high-energy electron diffraction (RHEED) pattern of an as-grown $MoSe_2$ (top image), in which the streaky patterns indicate a smooth 2D film. Upon annealing in vacuum for 30 minutes, a new set of dim and spotty patterns appears (pointed by the red arrows in the middle image) with the corresponding lattice constant being consistent with that of Mo_6Se_6, whose atomic structure is schematically shown in Figure 1b. It signifies the formation of Mo_6Se_6 nanowires and confirmed by subsequent STM and STEM measurements (Figure 1c and inset). The length of Mo_6Se_6 nanowires is found tunable by adjusting the annealing time and substrate temperature (see Supporting Information 1). The 1D Mo_6Se_6 nanowires can be converted back to $MoSe_2$ by annealing under Se at ~800 °C. In the RHEED, the spotty pattern disappears (see the lower image in Figure 1a), while the STEM and STM measurements (Figure 1d and inset) further assert the disappearance of the Mo_6Se_6 wires in the sample. Instead, many second or higher layers of $MoSe_2$ has formed at the edges of ML-$MoSe_2$ domains or islands (see Figure 1d and Supporting Information Figure S1h). Interestingly, it can happen that the newly formed $MoSe_2$ layer by selenization misaligns with that below, showing twist angles as large as 5.1° (Supporting Information Figure S1h inset).
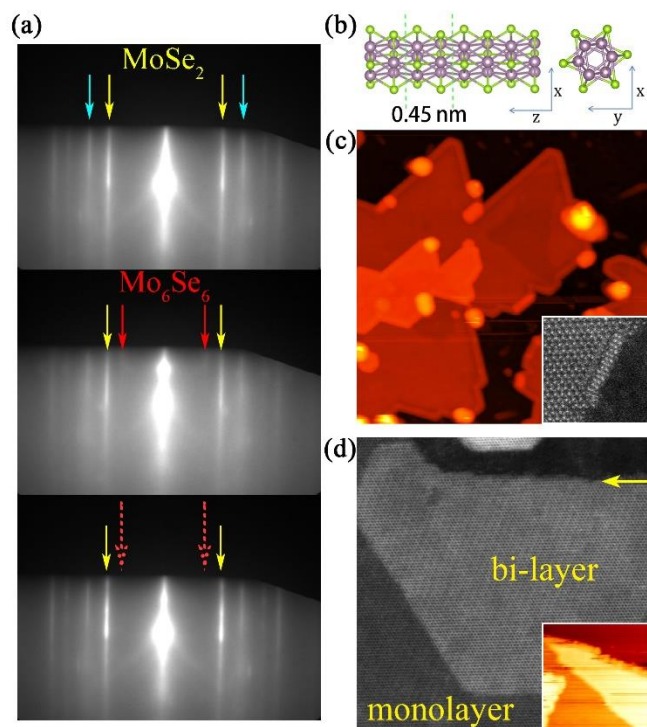
Figure 1. Formation and structure of Mo_6Se_6 nanowires. (a) RHEED patterns of an as-grown $MoSe_2$ film (top image, where yellow arrows point at patterns of $MoSe_2$ while the blue arrows point at that of graphene substrate), after annealing in vacuum for 30 minutes (middle image, where the red arrows point at diffraction patterns from Mo_6Se_6), and after selenization (lower image, in which the pattern of Mo_6Se_6 (marked by red dashed arrows) disappear). (b) Schematics of a single Mo_6Se_6 wire in both the side and end views (left and right, where the green balls denote Se atoms and the purple balls are Mo atoms). (c) STM (size: 100×100 nm^2, sample bias: 1.0 V) and ADF-STEM images (inset, size: 5×5 nm^2) showing Mo_6Se_6 nanowires formed at domain/island edges of $MoSe_2$. (d) ADF-STEM (size: 30×30 nm^2) and STM images (inset, size: 45×45 nm^2, sample bias: 1.0 V) showing the second-layer $MoSe_2$ formed at the edge of ML-$MoSe_2$ (marked by arrow) by selenization of the Mo_6Se_6-containing sample.

We note that Mo_6Se_6 nanowires preferentially form at the Se-terminated zigzag edges (Se-zz edges). We do not observe Mo_6Se_6 nanowires at Mo-terminated zigzag boundaries (Mo-zz edges) at early stage annealing. For example, Figure 2a shows a stripe of $MoSe_2$ ML with its left side (i.e., the Se-zz edge) terminated by segments of Mo_6Se_6 nanowires, whereas on the right side (Mo-zz edge), no Mo_6Se_6 wire is found. This behavior of edge-selective formation of Mo_6Se_6 nanowire has not been reported before. Similar M_6X_6 nanowires reportedly observed by TEM and induced by e-beam irradiation were indistinguishable at the two edges.[27, 28] Our observation of a preferential formation of Mo_6Se_6 nanowires at the Se-zz edge of $MoSe_2$ would thus suggest a kinetic pathway associated with the different thermal stability or atom desorption rates between the two edges. For example, because of the different number of chemical bonds per edge atoms, Se desorption or detachment from the Se-zz edge expectedly has a higher rate than that from the Mo-zz edge (Figure 2b). Therefore, during annealing, Se atoms will be more likely desorbed from the Se-zz edge, decreasing the local chemical potential of Se and facilitating the growth of the stoichiometric Mo_6Se_6 at the Se-zz edge. By DFT calculations, we further show that even at one and the same chemical potential, μ_{Se}, the Se edge is also more favorably converted to Mo_6Se_6 than the Mo edge. Figure 2c summarizes the DFT results of the formation energies of bare Se-zz and Mo-zz edges, and Mo_6Se_6 wires interfaced with $MoSe_2$ ML by the 5|8 or 4|4E structures respectively (the two interfaces are detailed below), as a function of Se chemical potential μ_{Se} (refer to Supporting Information 2 for calculation details). As seen, at low μ_{Se} (or high μ_{Mo}), the formation energy of Mo_6Se_6 is lower than that of both Se-zz and Mo-zz edges of $MoSe_2$, so both edges are unstable against transformation into Mo_6Se_6. On the other hand, the critical values of μ_{Se} at which Mo_6Se_6 becomes more favorable are different for the two

edges – it is higher for the Se-zz than the Mo-zz edge, therefore, when the environment becomes Se-poor by annealing the sample, the Se-zz edge of MoSe$_2$ will firstly transform to Mo$_6$Se$_6$. If, as elaborated above, the kinetics of Se desorption makes μ_{Se} at the Se-zz edge smaller than the Mo-zz edge, formation of Mo$_6$Se$_6$ at the Se edge may be pushed further, consistent with the experiment. Under high-energy electron bombardment during the TEM experiments, on the other hand, Se atoms are likely knocked out and desorbed at approximately equal rates from both edges and so M$_6$X$_6$ wires form more uniformly irrespective of the character of the step-edges.
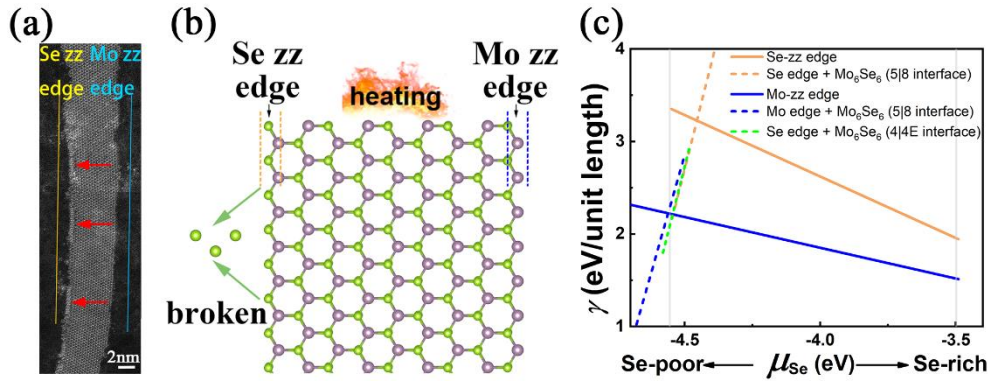
Figure 2. Preferential Mo$_6$Se$_6$ nanowire formation at Se-zigzag edge. (a) ADF-STEM image showing segments of Mo$_6$Se$_6$ nanowires (pointed by red arrows) at the Se edge of a ML-MoSe$_2$ domain. (b) Schematic illustration of Mo$_6$Se$_6$ nanowire formation preferentially at the Se-zz edge by annealing. (c) DFT calculated formation energies per unit cell (0.33 nm) of Se-zz and Mo-zz edges, with or without Mo$_6$Se$_6$ nanowires attached via the 5|8 or 4|4E structures, as a function of Se chemical potential μ_{Se}. The two vertical grey lines represent the range of μ_{Se} as set by the formation of bulk Se (-3.50 eV) and bulk Mo (-4.55 eV).

We have examined the interfaces between Mo_6Se_6 nanowire and the parent $MoSe_2$ ML sheet by atomic resolution ADF-STEM and found two typical structures, i.e., 5|8 and 4|4E structures. The former is characterized by alternating pentagon-octagon atom rings at the interface as shown in Figure 3a of an experimental ADF-STEM image and Figure 3b for the ball-and-stick model. The 4|4E interface has double 4-atom rings that share the Mo-Se bond at the edge on the $MoSe_2$ side of the interface (Figures 3d and 3e for an experimental ADF-STEM image and the ball-and-stick model, respectively). Simulated ADF-STEM images of the two interfaces based on the models of Figures. 3b and 3e are presented in Supporting Information 3. The 4|4E interface structure resembles that of mirror twin domain boundary in $MoSe_2$ ML and behaves as metal.[29] It would manifests by a bright contrast in STM and is indistinguishable from that of the attached metallic Mo_6Se_6 wire. So a featureless but uniform bright contrast is shown in Figure 3f. This contrasts to the 5|8 interface where the Mo_6Se_6 nanowire and $MoSe_2$ sheet are separated by a loose and a weak bonding region (only one of the six Se atoms in Mo_6Se_6 is directly linked with the Mo atoms in $MoSe_2$ domains). There exists a 'magic match' between 4 units of $MoSe_2$ along the zigzag direction and 3 unit cells of Mo_6Se_6, producing a Moiré pattern of size $3a_{Mo_6Se_6} \approx 4a_{MoSe_2}$, where $a_{Mo_6Se_6} \approx 0.45$ nm and $a_{MoSe_2} \approx 0.33$ nm. Correspondingly, the STM image of Figure 3c reveals not only the 5|8 ring-like feature at the interface but also an intensity undulation of periodicity $3a_{Mo_6Se_6}$, reflecting the Moiré pattern.
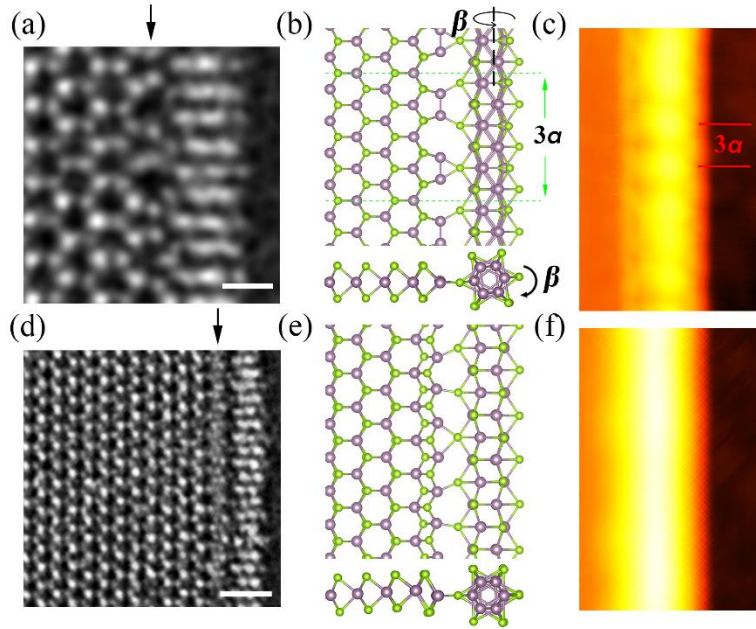
**Figure 3.** Two interfaces connecting Mo_6Se_6 nanowire and $MoSe_2$ ML sheet. (a,d) ADF-STEM images showing the interfaces (indicated by the black arrows) between Mo_6Se_6 wires (right and brighter part) and $MoSe_2$ ML domains (left region) having the 5|8 (a, scale bar: 0.5 nm) and 4|4E structures (d, scale bar: 1 nm). (b,e) Stick-and-ball models illustrating the 5|8 (b) and 4|4E (e) interface structures, respectively. The top panels are of top-views while the low panels are the end-views. (c,f) STM images (size: 5.4×8.3 nm^2) showing Mo_6Se_6 wires (middle bright regions) joining the $MoSe_2$ ML on the left with the 5|8 (c, bias: 0.5V) and 4|4E (f, bias: -1.0V) interface structures. The right dark regions in both images are of substrate. Note in (b,c), a is the lattice constant of Mo_6Se_6 unit cell.

Mo_6Se_6 nanowire is a metal. It is known that in 1D metals, low-energy excitations such as CDW may exist. For wires of finite lengths, quantum confinement effect is also expected. We have probed the electronic structures of Mo_6Se_6 wires interfaced with $MoSe_2$ by the 5|8 structure by low-temperature STS. The 5|8 interface is particularly chosen as it represents an electrically

more isolated 1D system. For one with the 4|4E interface, the Mo_6Se_6 wire and the 4|4E interface are both metals and electrically connected, ruining the 1D characteristics of the nanowires. In Figures 4a and 4b, we present STS spectra acquired on Mo_6Se_6 wires of different lengths (~8, ~14 and ~30 nm in Figure 4a, and ~47 nm in Figure 4b). A prominent difference between short ($\leq$ 30 nm) and long wires may be noted: for the short ones, apparent gaps are seen at the Fermi level (0 eV) and the gap size shrinks as the wire length increases. In fact, we find the gap size E_g is inversely proportional to the wire length L: $E_g \propto 1/L$ (Figure 4c). For long wires (> 30 nm), the gap is almost closed but an apparent suppression of the DOS at the Fermi level is still discernable. Because of the wire-length dependence of the E_g, we may rule out the Peierls-type CDW to be the cause of the DOS gaps in short wires. Indeed, our DFT calculations of the phonon modes of Mo_6Se_6 (see Supporting Information 4, Figure S4) indicate the wire to be stable against formation of the CDW. Instead, we suggest it is the charge gap of the TLL in short 1D wires. As will be noted in later discussions (Figure. 5), the DOS gap at E_F is extra larger than the quantum well gaps see at energies off the Fermi level. Together with the inverse-L dependence, it could well be explained by the quantum confined TLL, where the gap contains two contributions: the charging and quantum confinement effects.[6, 29, 30] For long wires, the power-law suppression of the DOS at E_F, i.e., $N(E) \sim |E|^\alpha$, where the exponent α relates to the Luttinger parameter K_C and reflects the strength of electron interaction in system,[31, 32] represents another signature of the TLL. A fit of the data over the energy range of −80 meV < E < 80 meV in Figure 4b by the above power law is indicated by the green dashed line, which results in an exponent of $\alpha \sim 0.75$.
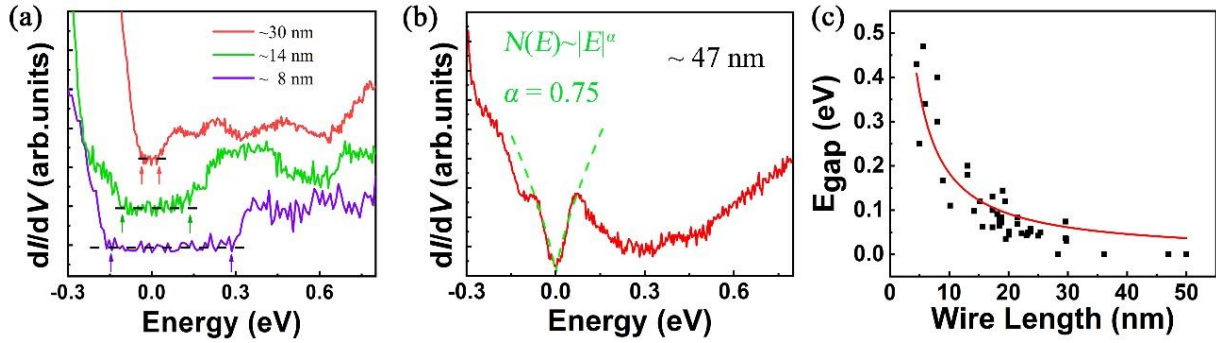
Figure 4. Electronic characteristics of Mo₆Se₆ nanowires of varying lengths. (a) STS spectra of Mo₆Se₆ nanowires of three different lengths (vertically shifted for clarity with the spectrum base being indicated by the horizontal black-dashed lines), showing DOS gaps of various sizes at the Fermi level. (b) STS spectrum of a ~47 nm nanowire showing no gap but a power-law DOS suppression at E_F. The green dashed line represents the best fit of the data by the power-law. (c) Dependence of the DOS gap as a function of Mo₆Se₆ wire length.

We have further looked at the quantum confined TTL in short wires (≤ 10 nm) by STS 'mapping' and Figures 5a and 5b show the energy-and-position dependent differential conductance 'maps' for two wires of lengths ~8 nm and ~5 nm, respectively. As seen, undulations of the conductance are apparent along the wires and at some selected energies, signifying the quantum well states (QWS). Several prominent features are observed in the data: (1) consistent with the spectra in Figure 4a above, there exists an extra energy gap around E_F and its size is greater in the shorter wire. The gap around E_F is notably larger than the quantum gaps away from E_F; (2) For the empty states ($E > E_F$), it is hole-like where the undulation frequency (or wave vector k) decreases with increasing energy. For the filled states ($E < E_F$), on the other

hand, although only one set of undulations are observable, the undulation period deviates from that extrapolated from high energy and it is more electron-like (e.g., it is reduced from 5 to 4 as the energy decreases from 0.4 eV above E_F to -0.2 eV below E_F in Figure 5a); (3) there are extra sets of undulations, which have the same periods and in-phase relations with that at the neighboring energy (e.g., the undulations at ~0.5 eV and ~0.4 eV in Figure 5b). This may signify spin-charge separation of the TLL in real space.[29, 32]

To better understand these features, we make reference to the DFT calculated electronic band and the DOS of *freestanding* Mo_6Se_6 (Figure 5c). We note firstly that a freestanding Mo_6Se_6 wire is metallic with the Fermi level deep in a band of high DOS. Over an energy range above the E_F (i.e., from ~0.3 eV to ~1.5 eV), it has a very low DOS, which corresponds to the dispersive band structure having two branches: the hole-like branch above $E \sim 1.0$ eV and electron-like branch below. Experimentally, the Fermi level has shifted upwards likely due to the effect of the substrate and neighboring $MoSe_2$. By comparing the calculated DOS (Figure 5c, right panel) and the STS taken from a long wire and over a wider energy range (Figure 5d), we note an overall agreement and the low DOS in Figure 5c corresponds to the energy range between ~0.2 eV and ~1.4 eV in the experiment. However, in the experimental spectra scanned over a smaller energy range, suppression of the DOS at the Fermi energy are apparent (see, e.g., Figure 4b above) due to effects not accounted for in the DFT calculations. Figure 5d inset presents the STS map from a long Mo_6Se_6 wire where quantum confinement is minimal.

From Figures 5a and 5b, one may derive the wave-vectors k of the quantized states by measuring the charge density undulation periods. They are found to be close to $\frac{1}{3}\left(\frac{\pi}{a}\right)$, i.e., one-

third of half Brillouin zone. From Figure 5c, one however finds no state at $k \sim \frac{1}{3}\left(\frac{\pi}{a}\right)$ that can

give rise to the dispersion reflected by the experimentally observed QWS in Figures 5a and 5b. Instead, the hole-like and electron-like dispersive bands, which seem to correlate well with the experiment (i.e., feature 2 described above), are at much higher k values close to the BZ

boundary $Z = \left(\frac{\pi}{a}\right)$. To explain this, we note the $3a$ Moiré patterns existed in the system (refer

to Figure 3c), which may modify the electron structure of the system. To evaluate the Moiré effect, we have performed additional DFT calculations of a simple model where a larger period of $3a$ is artificially introduced along the Mo_6Se_6 wire (see Supporting Information 5). The results show that the highly dispersive bands close to Z retain but become folded in a reduced Brillouin zone (BZ) of width $\Gamma Z / 3$. Mini-gaps are also opened for the folded bands at the reduced BZ boundary $k' = \Gamma Z / 3$ (see Figure S5d). This appears consistent with the experiment. Nevertheless, we would like to stress that the model is rather oversimplified (e.g., the effects of the connected $MoSe_2$ and the substrate are completely ignored). Besides, the adequacy of DFT in dealing with such strongly correlated systems may also be questionable. Further studies will be needed to account for all the details and subtleties of the experiment.
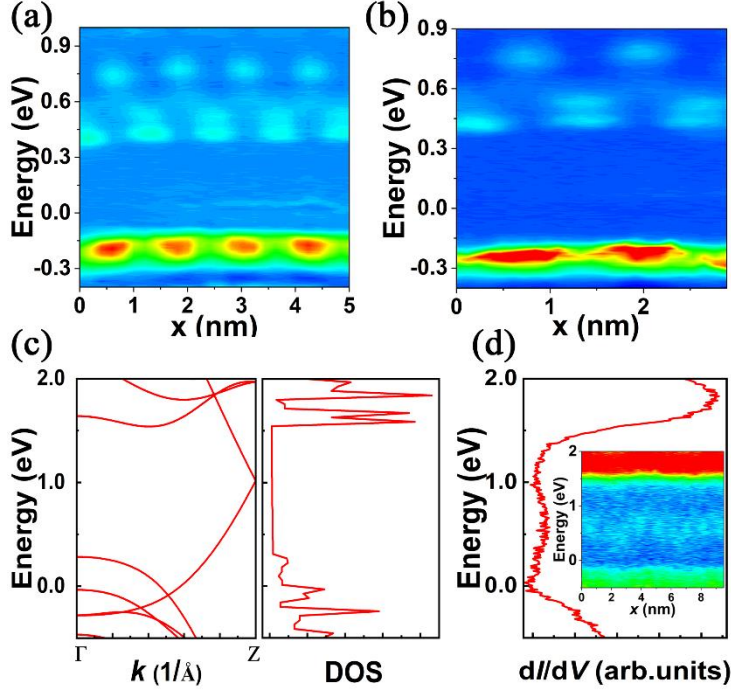
Figure 5. Quantum well states in short Mo_6Se_6 nanowires. (a,b) Spatially-resolved STS maps of Mo_6Se_6 nanowires of lengths (a) ~8 nm and (b) ~5 nm. (c) DFT calculated energy band (left) and the DOS (right) of a freestanding Mo_6Se_6 nanowire. (d) STS spectrum (averaged over 10 spectra) of a ~30 nm long Mo_6Se_6 nanowire. The inset is a STS-map of the same wire.

To conclude, we have obtained 1D Mo_6Se_6 nanowires by annealing of epitaxial $MoSe_2$ monolayer after its growth by MBE, which represents a new and highly controllable method of 1D Mo_6Se_6 nanowires fabrication. The Mo_6Se_6 nanowires can be converted back to $MoSe_2$ upon selenization at high temperature. The Mo_6Se_6 nanowires form preferentially at Se-terminated zigzag edges of $MoSe_2$ during early stage of annealing and stitch with $MoSe_2$ by two atomic configurations – the 5|8 rings and the 4|4E boundaries. Mo_6Se_6 wires are metals, exhibiting DOS suppression at the Fermi level for long wires and DOS gaps for short wires. For the latter, the

size of the energy gap depends inversely on the wire-length, which is inconsistent with the CDW. On the other hand, a power-law DOS suppression at E_F and the wire-length dependent gaps are in agreement with quantum confined TLL.

ASSOCIATED CONTENT

Supporting Information

The formation processes of Mo_6Se_6 nanowires, DFT calculation on the edge formation energies, QSTEM simulated images of two interface structures, the phonon spectrum of Mo_6Se_6 nanowires, Moiré effect on electronic structure of Mo_6Se_6 wires and experimental methods.

AUTHOR INFORMATION

Corresponding Authors

* Email: mhxie@hku.hk (MHX); chhjin@zju.edu.cn (CHJ).

Author Contributions

M.X. and C.J. conceived and coordinated this work. Y.X. and J.Z. performed the MBE growth and STM/S experiments. B.W. conducted the ADF-STEM measurements. Y.J. and H.T. carried out the theoretical calculations with the supervision from H.X. W.H. provided technical support and participated in the discussions. Y.X., B.W. and J.Z contributed equally to this work.

Funding Sources

Notes

The authors declare no competing financial interest.

ACKNOWLEDGEMENTS

REFERENCE

1.   Ishii, H.; Kataura, H.; Shiozawa, H.; Yoshioka, H.; Otsubo, H.; Takayama, Y.; Miyahara, T.; Suzuki, S.; Achiba, Y.; Nakatake, M. *Nature* **2003,** 426, (6966), 540.

2.   Egger, R.; Gogolin, A. O. *Physical review letters* **1997,** 79, (25), 5082.

3.   Kane, C.; Balents, L.; Fisher, M. P. *Physical review letters* **1997,** 79, (25), 5086.

4.   Yao, Z.; Postma, H. W. C.; Balents, L.; Dekker, C. *Nature* **1999,** 402, (6759), 273.

5.   Li, T.; Wang, P.; Fu, H.; Du, L.; Schreiber, K. A.; Mu, X.; Liu, X.; Sullivan, G.; Csáthy, G. A.; Lin, X. *Physical review letters* **2015,** 115, (13), 136804.

6.   Auslaender, O.; Steinberg, H.; Yacoby, A.; Tserkovnyak, Y.; Halperin, B.; Baldwin, K.; Pfeiffer, L.; West, K. *Science* **2005,** 308, (5718), 88-92.

7.   Jompol, Y.; Ford, C.; Griffiths, J.; Farrer, I.; Jones, G.; Anderson, D.; Ritchie, D.; Silk, T.; Schofield, A. *Science* **2009,** 325, (5940), 597-601.

8.   Yacoby, A.; Stormer, H.; Wingreen, N. S.; Pfeiffer, L.; Baldwin, K.; West, K. *Physical review letters* **1996,** 77, (22), 4612.

9.   Blumenstein, C.; Schäfer, J.; Mietke, S.; Meyer, S.; Dollinger, A.; Lochner, M.; Cui, X.; Patthey, L.; Matzdorf, R.; Claessen, R. *Nature Physics* **2011,** 7, (10), 776.

10.   Venkataraman, L.; Hong, Y. S.; Kim, P. *Phys Rev Lett* **2006,** 96, (7), 076601.

11.   Claessen, R.; Sing, M.; Schwingenschlögl, U.; Blaha, P.; Dressel, M.; Jacobsen, C. S. *Physical review letters* **2002,** 88, (9), 096402.

12.   Yeom, H. W.; Takeda, S.; Rotenberg, E.; Matsuda, I.; Horikoshi, K.; Schaefer, J.; Lee, C.; Kevan, S.; Ohta, T.; Nagao, T. *Physical review letters* **1999,** 82, (24), 4898.

13.   Ahn, J.; Byun, J.; Koh, H.; Rotenberg, E.; Kevan, S.; Yeom, H. *Physical review letters* **2004,** 93, (10), 106401.

14.   Ahn, J. R.; Yeom, H. W.; Yoon, H. S.; Lyo, I. W. *Physical Review Letters* **2003,** 91, (19), 196403.

15.   Luttinger, J. *Physical Review* **1960,** 119, (4), 1153.

16.   Voit, J. *Reports on Progress in Physics* **1995,** 58, (9), 977.

17.   Mattsson, A. E.; Eggert, S.; Johannesson, H. *Physical Review B* **1997,** 56, (24), 15615-15628.

18.   Kane, C. L.; Fisher, M. P. *Phys Rev Lett* **1992,** 68, (8), 1220-1223.

19.   Bockrath, M.; Cobden, D. H.; Lu, J.; Rinzler, A. G.; Smalley, R. E.; Balents, L.; McEuen, P. L. *Nature* **1999,** 397, (6720), 598-601.

20.   Gao, B.; Komnik, A.; Egger, R.; Glattli, D. C.; Bachtold, A. *Phys Rev Lett* **2004,** 92, (21), 216804.

21.   Hager, J.; Matzdorf, R.; He, J.; Jin, R.; Mandrus, D.; Cazalilla, M.; Plummer, E. W. *Physical review letters* **2005,** 95, (18), 186402.

22.   Wang, F.; Alvarez, J.; Mo, S.-K.; Allen, J.; Gweon, G.-H.; He, J.; Jin, R.; Mandrus, D.; Höchst, H. *Physical review letters* **2006,** 96, (19), 196403.

23.   Ma, Y.; Diaz, H. C.; Avila, J.; Chen, C.; Kalappattil, V.; Das, R.; Phan, M.-H.; Čadež, T.; Carmelo, J. M.; Asensio, M. C. *Nature communications* **2017,** 8, 14231.

24.   Xia, Y.; Wang, B.; Zhang, J.; Feng, Y.; Li, B.; Ren, X.; Tian, H.; Xu, J.; Ho, W.; Xu, H. *2D Materials* **2018,** 5, (4), 041005.

25.   Chang, A. *Reviews of Modern Physics* **2003,** 75, (4), 1449.

26.   Stühler, R.; Reis, F.; Müller, T.; Helbig, T.; Schwemmer, T.; Thomale, R.; Schäfer, J.; Claessen, R. *Nature Physics* **2019**.

27.   Huang, W.; Wang, X.; Ji, X.; Zhang, Z.; Jin, C. *Nano Research* **2018,** 11, (11), 5849-5857.

28.   Sang, X.; Li, X.; Zhao, W.; Dong, J.; Rouleau, C. M.; Geohegan, D. B.; Ding, F.; Xiao, K.; Unocic, R. R. *Nature communications* **2018,** 9, (1), 2051.

29.   Jolie, W.; Murray, C.; Weiß, P. S.; Hall, J.; Portner, F.; Atodiresei, N.; Krasheninnikov, A.

V.; Busse, C.; Komsa, H.-P.; Rosch, A.; Michely, T. *Physical Review X* **2019,** 9, (1), 011055.

30.   Hashisaka, M.; Hiyama, N.; Akiho, T.; Muraki, K.; Fujisawa, T. *Nature Physics* **2017,** 13, 559.

31.   Eggert, S. *Phys Rev Lett* **2000,** 84, (19), 4413-6.

32.   Lee, J.; Eggert, S.; Kim, H.; Kahng, S.-J.; Shinohara, H.; Kuk, Y. *Physical review letters* **2004,** 93, (16), 166403.

Supporting Information

Quantum confined Tomonaga-Luttinger liquid in Mo$_6$Se$_6$ nanowires converted from epitaxial MoSe$_2$ monolayer

Yipu Xia,[†,‡] Bo Wang,[∥,‡] Junqiu Zhang,[†,‡] Yuanjun Jin,[†,§] Ho Tian,[†,§] Wingkin Ho,[†] Hu Xu,[§] Chuanhong Jin[∥,] and Maohai Xie[†,*]*

[†]Physics Department, the University of Hong Kong, Pokfulam Road, Hong Kong

[∥]State Key Laboratory of Silicon Materials, School of Materials and Engineering, Zhejiang University, Hangzhou, Zhejiang, 310027, China

[§]Department of Physics, Southern University of Science and Technology, Shenzhen, Guangdong 518055, China

[‡]These authors contributed equally to this paper.

[*]Corresponding authors, Emails: chhjin@zju.edu.cn (CHJ), mhxie@hku.hk (MHX).

1. Formation processes of Mo_6Se_6 nanowires

Figures S1a-c present a set of STM images revealing the formation process of Mo_6Se_6 nanowires by increasing the annealing time but at a fixed temperature of ~800°C. The $MoSe_2$ film was pre-grown by MBE on the SiC-supported graphene substrate. As seen, at the early stage of annealing (Figure S1a), short wires emerge at the boundaries of $MoSe_2$ islands or domains. They lengthen with increasing annealing time (Figure S1b) and eventually the whole edge of ML $MoSe_2$ island or domain becomes converted into Mo_6Se_6 (Figure S1c). Combining atomic resolution STM (e.g., Figure S1c inset) and annular dark-field (ADF) STEM (Figures S1d-f), we establish the atomic structure of the nanowires to be Mo_6Se_6, which is as sketched in Figure 1b in the main text. In most cases, individual Mo_6Se_6 nanowires are seen at $MoSe_2$ island or domain boundaries. In other cases, especially those under prolonged and high-temperature annealing, double, triple (Figure S1e) and even bundles (Figure S1f) of Mo_6Se_6 nanowires could form by completely dissolving a $MoSe_2$ patch or island. The Mo_6Se_6 wires in the bundle lie parallel on substrate surface. Fourier transform (FT) of Figure S1f shows, besides spots corresponding to $MoSe_2$ lattices, features of the Mo_6Se_6 bundle stacked parallel with an inter-wire distance of ~0.82 nm (blue circles in the inset). From the diffraction spots marked by the red circles, we further derive that the lattice constant of Mo_6Se_6 along its length is ~0.45nm (note that the FT of a top-view image of Mo_6Se_6 reflects half of the unit cell size), consistent with our density-functional theory (DFT) calculations of the lattice constants. From Figure 1c in the main text, one may also note that some Mo_6Se_6 nanowires have formed even at the edges of the second layer $MoSe_2$, suggesting that Mo_6Se_6 wire formation out of $MoSe_2$ is not much associated with the identity of the substrate or the lattice registry of $MoSe_2$ with respect to the substrate. Once formed, these Mo_6Se_6 nanowires are very stable, which can withstand both high-temperature annealing (up to ~950°C) and exposure to ambient for more than one week.

By annealing the $MoSe_2$-Mo_6Se_6 sample under a flux of Se at temperature ~800°C, the Mo_6Se_6 nanowires will dissolve (Figure S1g). In addition, some second or higher layer $MoSe_2$ appear at the edges of ML-$MoSe_2$ domain or islands (Figure S1h). Different from direct epitaxial growth of $MoSe_2$, where the higher layers usually nucleate at the domain centers, the new $MoSe_2$ islands formed by selenization are close to the edges of ML-$MoSe_2$ domains, which are thus likely caused by the dissolving or reorganizing the 1D Mo_6Se_6 wire. Interestingly, the top $MoSe_2$ layer can be twisted relative to the bottom layer(s) with the twist angles as high as 5.1° (Figure S1h inset).

Figures S1i show two kinds of edges after selenization: one is zigzag Se edge (left) with a grain boundary like defect embedded next to the edge (marked by white rhombi), the other is zigzag Mo edge (right). Both edges are readily saturated by adsorption of Se atoms.
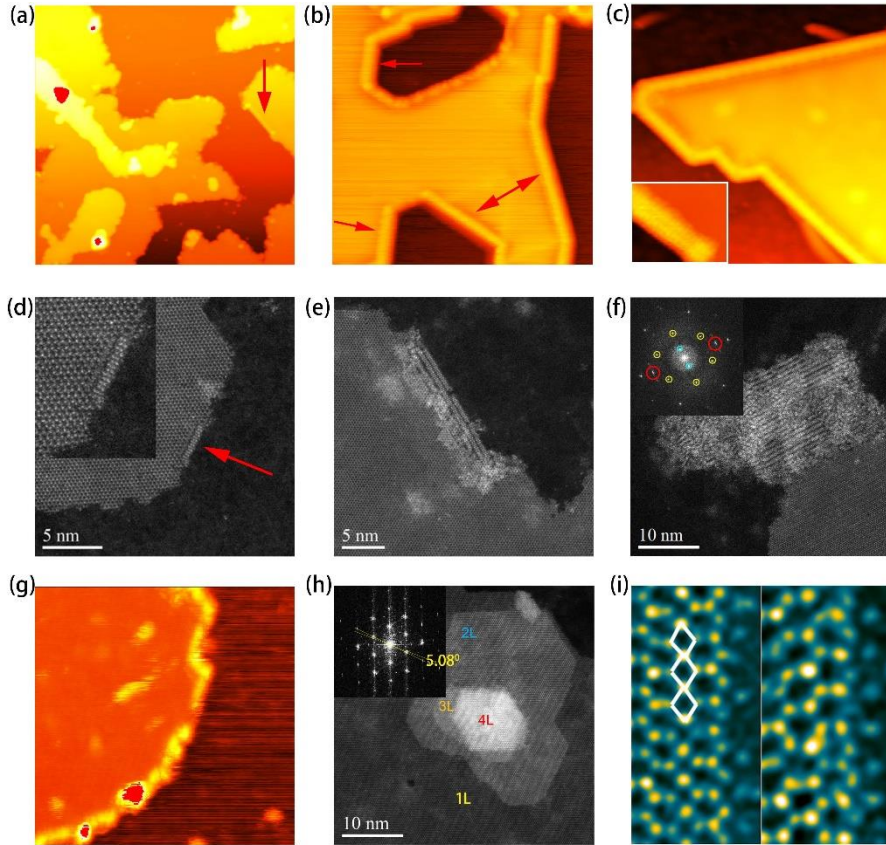
Figure S1. Formation and reversion of Mo_6Se_6 nanowires. a-c, STM images showing the gradual formation of Mo_6Se_6 nanowires with increasing annealing time from ~1 to ~30 minutes (size and sample bias of the images: (a) 100×100 nm^2, 2.0 V; (b) 50×50 nm^2, 1.0 V; (c) 30×30 nm^2, 0.5 V; inset of (c) 7.0×5.8 nm^2, 0.1 V). d-f, ADF-STEM images showing single, double and bundled Mo_6Se_6 nanowires. Inset of (f): FT of (f) revealing the frequency spectra of $MoSe_2$ (circled yellow) and Mo_6Se_6 (circled red for unit cell and blue for inter-wire) lattices. g, STM image (30×30 nm^2, sample bias: -1.0 V) of a Mo_6Se_6-containing sample after selenization. h, ADF-STEM image of the Mo_6Se_6-containing sample after selenization showing multiple $MoSe_2$ layers. Inset is the FT of the main figure revealing twist of the stacked $MoSe_2$ layers. i, ADF-STEM images of two kinds of edges after selenization. Left: ZZSe-GB4-Se structure (image size: 1.3×2.6 nm^2); right: ZZMo-Se structure (image size: 1.2×2.4 nm^2). The white rhombi in the left image mark grain boundary-like defects. In both, the edges are terminated by adsorbed Se atoms (the rightmost row of atoms).

2. DFT calculations of the edge formation energies as function of chemical potential

When considering the stabilities of different edge configurations, a ribbon is adopted to simulate a ML-$MoSe_2$ terminated by different edges for the DFT calculations. A clean ribbon has two complementary edges: Se-zz and Mo-zz. However, the as cleaved edges are energetically unfavorable, which undergo relaxation and reconstruction. Previous works[1-3] have suggested the Mo-zz edge is more likely saturated by Se atoms (refer to Figure S2-1a), whereas the Se-zz edge atoms undergo a reconstruction such that every other Se pair (one on

the top and the other on the bottom layer) forms bond, giving rise to the 2× periodicity (refer to Figure S2-1c). We adopt these two configurations for the two edges and calculated separately their formation energies γ using triangular domains bounded by one of the edges (e.g., Figure S2-2 for the Se-zz case). The formation energy ($E_f{'}$) of the triangular domain then consists of two parts – the creation of the edges (γ) and that of the vertices of the triangle (ε_v):

$$E_f{'} = 3\varepsilon_v + 3l\gamma$$

To separate the two contributions, three sizes of triangular domains with changing edge lengths (l) but fixed 3 vertices are considered, thereby the vertex contribution is readily eliminated and the energy γ obtained by simply fitting the $E_f(l)$ relation.

To calculate the formation energy of Mo_6Se_6 attached to either Mo-zz or Se-zz, a $MoSe_2$ ribbon with one edge connected to Mo_6Se_6 while the other edge takes the relaxed and reconstructed configuration retaining the $MoSe_2$ stoichiometry is adopted. These are depicted in Figure S2-1b and S2-1d, respectively. The latter represents one that is consistent with the experiment (refer to Figure 2 and the discussions in main text). Another configuration that is also seen by experiment is Mo_6Se_6 wires attached to Se-zz edge of $MoSe_2$ by the 4|4E interface structure (see Figure 2e in the main text). Its formation energy is calculated in a similar way as that of Figure S2-1d. Note that for the spectator Mo-edge, the reconstructed configuration adopted in Figure S2-1d is less favorable than that of a Se-saturated edge (cf. Figure S2-1a), but this is irrelevant in deriving the energy of Mo_6Se_6 wire, as long as its energy is separately taken into account as derivable by considering again triangular domains of Figure S2-3.

The formation energy E_f of the system (ribbon with the Se- and Mo-terminated edges or that with one edge connected to a Mo_6Se_6 wire) depends on Se chemical potential μ_{Se} according to

$$E_f = E(Mo_xSe_y) - xE_0 + (2x - y)\mu_{Se}$$

where E_0 is the energy of one $MoSe_2$ unit, $x(y)$ is the overall composition of Mo(Se) atoms in the system, and $(2x - y)$ represents the 'excess' of Se in the system than is required in forming a stoichiometric $MoSe_2$. The formation energy of the interested edges or Mo_6Se_6, γ, is then

$$\gamma = E(Mo_xSe_y) - xE_0 + (2x - y)\mu_{Se} - \gamma_s$$

with γ_s being the energy of the 'spectator' edge on the opposite side.

One thing to address is that our MBE-grown Mo_6Se_6 nanowire has a rotation angle of $\beta = 30°$ about the c-axis (refer to Figure 2b) instead of $\beta = 0°$ reported in the literature.[4, 5] Note that the $30°$ rotation angle would result in a weaker bonding between Mo_6Se_6 and the host $MoSe_2$ (only one of the six Se atoms in Mo_6Se_6 is directly linked with the Mo atoms in $MoSe_2$ domains), which would then impact on the properties of the Mo_6Se_6 wires. However, in the DFT simulations of freestanding models (without considering the substrate), such rotation angel is not stable

and would rotate to $\beta = 0°$ after relaxation. We thus suspect that the experimentally observed rotation angle of $\beta = 30°$ may be associated with the graphene or HOPG substrates.
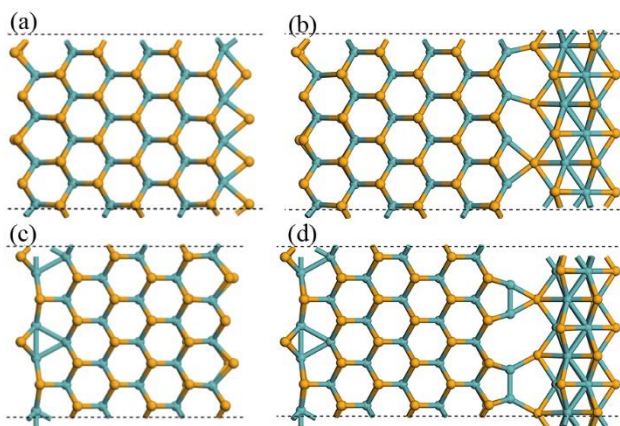
Figure S2-1. Models of ribbons constructed to calculate the formation energies of the edges with or without the Mo_6Se_6 wire as functions of Se chemical potential. The yellow balls denote Se atoms and the cyan balls are Mo atoms. (a) and (b) are the optimized Mo edge and a Mo_6Se_6 wire attached to Mo-edge, respectively. The 'spectator' edge on the left side of the ribbon is the ×2 reconstructed Se-zz edge. (c) and (d) are optimized Se edge and a Mo_6Se_6 attached to the Se-edge, respectively. The 'spectator' edge on the left is a relaxed and reconstructed Mo-zz without changing stoichiometry. Model (d) is identified to be consistent with the experiment shown in Figure 2 in the main text.
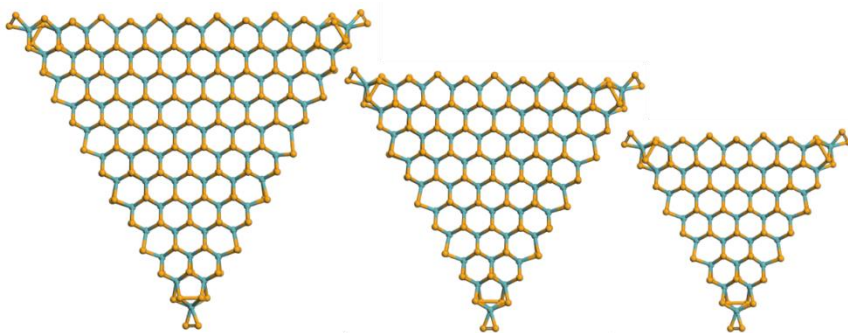

Figure S2-2. Models of triangular domains bounded by the Se-zz edges, which are adopted in calculating the formation energy of the Se terminated edge.
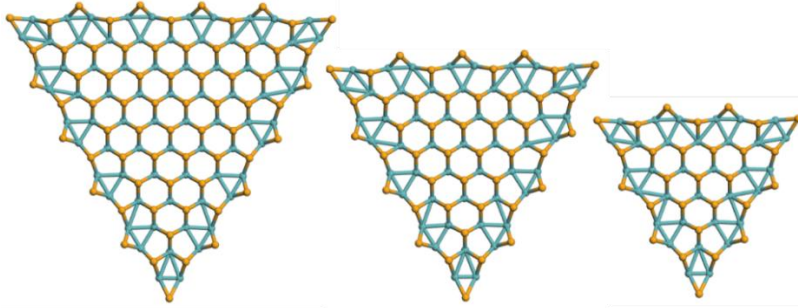
Figure S2-3. Models of triangular domains bounded by the Mo-zz edges adopted in calculating the formation energy of the Mo terminated 'spectator' edge.

3. Two interface structures connecting Mo₆Se₆ and MoSe₂

We found two typical interface structures, i.e., 5|8 and 4|4E, connecting Mo_6Se_6 nanowire and $MoSe_2$ ML sheet. The former is characterized by alternating pentagon-octagon atom rings at the interface (see Figures 3a-3c in the main text), where Mo_6Se_6 wire and $MoSe_2$ sheet stitch together loosely. Figure S3a presents the QSTEM simulated image of the 5|8 interface (the $MoSe_2$ domain is on left and Mo_6Se_6 nanowire is on right) based on the structure of Figure 3b, which is seen to match well with the experimental STEM result (Figure 3a in main text). Different from the previously reported electron-irradiation-induced Mo_6Se_6 nanowires, our MBE-grown Mo_6Se_6 nanowire has a rotation angle of $\beta = 30°$ about the c-axis (refer to Figure 3b in the main text) instead of $\beta = 0°$ reported in the literature.[4, 5] The 30-degree rotation angle would result in a weaker bonding between Mo_6Se_6 and $MoSe_2$ (only one of the six Se atoms in Mo_6Se_6 is directly linked with the Mo atoms in $MoSe_2$ domains), which would impact on the properties of the Mo_6Se_6 wires. For the second, 4|4E, interface structure, it has double 4-atom rings that share the Mo-Se bond at the edge on the $MoSe_2$ side of the interface (see Figures 3d-3f in the main text). Figure S3b shows a QSTEM simulated ADF-STEM image of such a model structure, which again agrees with the experimental observation (Figure 3d in the main text).
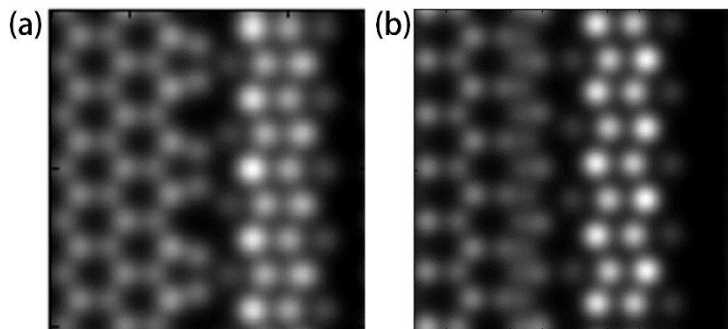

Figure S3. QSTEM simulated images of the two interface structures. a, 5|8 interface. b, 4|4E interface. The left part showing low contrast in each image are the $MoSe_2$ domains and the right bright region represents the Mo_6Se_6 nanowires.

4. Phonon spectrum of Mo$_6$Se$_6$ nanowires

Under low temperature, some 1D metallic systems may exhibit Peierls instability, which causes periodic lattice distortion and charge density wave (CDW). Phonon spectrum calculated by DFT can be helpful in identifying the existence of such CDW in 1D. Figure S4 shows the calculated phonon spectrum of freestanding Mo$_6$Se$_6$ nanowires. As seen, there is no imaginary frequency, which indicates the unlikelihood of Peierls-type CDW in the system.
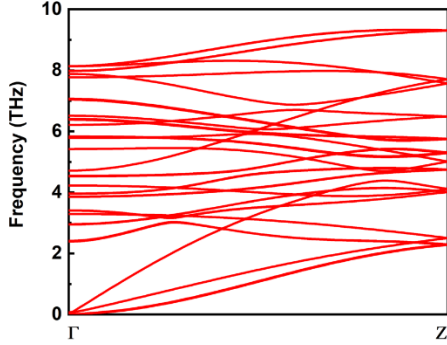
Figure S4. Phonon spectrum of Mo$_6$Se$_6$ nanowires.

5. Moiré effect on electronic structure of Mo$_6$Se$_6$ wires

For a MoSe$_2$ attached Mo$_6$Se$_6$ wire as shown in Fig. 3c, a Moiré modulation is present. This will bring an important effect on the electronic structure, such as energy band dispersion relation, of the Mo$_6$Se$_6$ wire. For example, for a small Moiré potential, an energy gap may be opened at wavevectors corresponding to the $3a$ periodicity, while the dispersion relation is more or less retained. In the case of strong Moiré potentials, however, the dispersion might be significantly altered or ruined. To evaluate the impact of the Moiré potential in the system, we performed DFT calculations of an oversimplified but manageable model, where an isolated Mo$_6$Se$_6$ wire is artificially distorted by ~1.65×10^{-2} nm, or 1.25%, for every 3 lattice units along the wire, thus a larger period of $3a$ is artificially introduced corresponding to the experiment. The calculation result is shown in Fig. S5(a) and S5(b). Comparing to the undistorted wire (Fig. 5c in the main text), there are extra bands, which originate from the band folding effect. Indeed, the $3a$ super-periodicity of the lattice reduces the Brillouin zone (BZ) size from $2\pi/a$ to $2\pi/3a$ and the bands are folded into the reduced zone. In particular, the highly dispersive bands close to the original BZ boundary becomes folded into the reduced-BZ close to the boundary $k' = \Gamma Z/3$. Besides, the Moiré potential has led to opening of mini-gaps of the folded bands at the reduced-BZ boundary k' (circled in (b)).
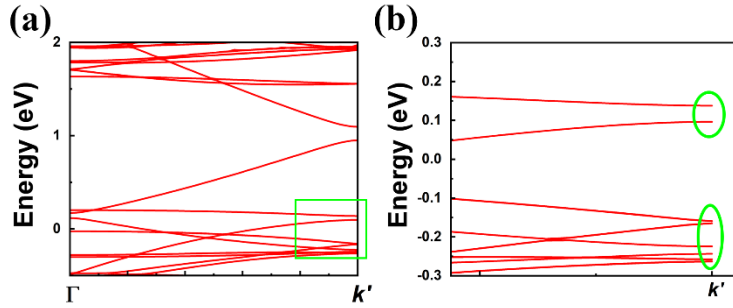
Figure S5. Moiré effect on the band structure of Mo_6Se_6 wire, where a super-periodic (periodicity 3a) lattice distortion ($\sim 1.65 \times 10^{-2}$ nm or 1.25%) is introduced along the wire. (a) DFT calculated band structure in half of the reduced Brillouin zone $\Gamma \rightarrow k'$, where $k' = \Gamma Z/3$. (b) Magnified plot of the boxed region of the band, where the circles highlight the folded bands with mini-gaps opened by the Moiré potential.

6. Experimental methods

Growth of nanowires

The growth of $MoSe_2$ thin films was carried out in an MBE chamber having a background pressure of 10^{-10} Torr. The flux of molybdenum was generated from an e-beam evaporator operated at the power of ~ 50 W, and that of selenium was generated from a Knudsen cell held at $\sim 125°C$. HOPG or epitaxial graphene were used as the substrates, where the latter was obtained by annealing SiC wafer at $\sim 1100°C$ under a Si flux. The temperature of the substrate was $\sim 500°C$ during $MoSe_2$ growth and the growth rate was ~ 0.5 MLs/hr as limited by the flux of Mo ($\sim 1.5 \times 10^{11}$ atoms/cm²·s). Se flux ($\sim 1.2 \times 10^{12}$ molecules/cm²·s) was around 10 times higher than that of Mo. Mo_6Se_6 nanowires were obtained by post-growth annealing at temperatures $\geq 800°C$. The length and coverage of the nanowires could be controlled by adjusting the annealing time (normally 1-30 mins). The growing surface was monitored by reflection high-energy electron diffraction (RHEED) operated at 15 keV.

STM and STEM Characterizations

The grown samples were transferred to a standalone Unisoku STM system for the STM/STS measurements at $\sim 5K$ and under the base pressure around 1×10^{-10} Torr. Constant current mode of scanning was used with the tunneling current of 100pA. The dI/dV spectra were taken by a lock-in amplifier at 1.009 kHz. Samples for ADF-STEM characterizations were transferred onto a molybdenum-based TEM grid via micromechanical exfoliation as reported in ref [6]. Atomic-resolution ADF-STEM were performed in a probe-corrected STEM (FEI Titan Chemi STEM) operated at 200 kV. The convergence semi-angle was set at 21.4 mrad and the range of acceptance angle of the ADF detector was 53-200 mrad. ADF-STEM image simulations were performed by the QSTEM software with the simulation parameters chosen to be the same as those used experimentally.[7]

DFT calculations

First-principles calculations were carried out using the Vienna ab initio simulation package (VASP), based on the density functional theory (DFT).[8] The interactions of electrons and the core are treated by projector augmented wave (PAW) method, with the cutoff energy 500 eV.[9] The Perdew-Burke-Ernzerhof (PBE) formalism of generalized gradient approximation (GGA)[10] was used for exchange-correlation. The k-point mesh of BZ was set to be $5 \times 1 \times 1$ in the self-consistency cycle. A $5 \times 1 \times 1$ supercell was constructed to obtain the phonon spectrum by using the PHONONPY code with the DFPT method.[11]

REFERENCE

1.   Chen, Y.; Cui, P.; Ren, X.; Zhang, C.; Jin, C.; Zhang, Z.; Shih, C.-K. *Nature Communications* **2017,** 8, (1), 15135.

2.   Helveg, S.; Lauritsen, J. V.; Lægsgaard, E.; Stensgaard, I.; Nørskov, J. K.; Clausen, B. S.; Topsøe, H.; Besenbacher, F. *Physical Review Letters* **2000,** 84, (5), 951-954.

3.   Bollinger, M. V.; Lauritsen, J. V.; Jacobsen, K. W.; Nørskov, J. K.; Helveg, S.; Besenbacher, F. *Physical Review Letters* **2001,** 87, (19), 196803.

4.   Sang, X.; Li, X.; Zhao, W.; Dong, J.; Rouleau, C. M.; Geohegan, D. B.; Ding, F.; Xiao, K.; Unocic, R. R. *Nature communications* **2018,** 9, (1), 2051.

5.   Huang, W.; Wang, X.; Ji, X.; Zhang, Z.; Jin, C. *Nano Research* **2018,** 11, (11), 5849-5857.

6.   Hong, J.; Wang, C.; Liu, H.; Ren, X.; Chen, J.; Wang, G.; Jia, J.; Xie, M.; Jin, C.; Ji, W.; Yuan, J.; Zhang, Z. *Nano Letters* **2017,** 17, (11), 6653-6660.

7.   Koch, C. T., *Determination of core structure periodicity and point defect density along dislocations*. 2002.

8.   Kresse, G.; Furthmüller, J. *Physical review B* **1996,** 54, (16), 11169.

9.   Blöchl, P. E. *Physical review B* **1994,** 50, (24), 17953.

10.   Perdew, J. P.; Burke, K.; Ernzerhof, M. *Physical review letters* **1996,** 77, (18), 3865.

11.   Togo, A.; Tanaka, I. *Scripta Materialia* **2015,** 108, 1-5.